Effects of heating temperature and atmosphere on element distribution and microstructure in high-Mn/Al austenitic low-density steel

Qi Zhang, Guanghui Chen, Yuemeng Zhu, Zhengliang Xue, and Guang Xu

View the article online at SpringerLink or IJMMM Webpage.

Articles you may be interested in

Jing Ma, Fan Feng, Bai-qing Yu, Hai-feng Chen, and Li-feng Fan, Effect of cooling temperature on the microstructure and corrosion behavior of X80 pipeline steel, *Int. J. Miner. Metall. Mater.*, 27(2020), No. 3, pp. 347-353. https://doi.org/10.1007/s12613-019-1882-x

Li Wang, Chao-fang Dong, Cheng Man, Ya-bo Hu, Qiang Yu, and Xiao-gang Li, Effect of microstructure on corrosion behavior of high strength martensite steel—A literature review, *Int. J. Miner. Metall. Mater.*, 28(2021), No. 5, pp. 754-773. https://doi.org/10.1007/s12613-020-2242-6

Yi-li Dai, Sheng-fu Yu, An-guo Huang, and Yu-sheng Shi, Microstructure and mechanical properties of high-strength low alloy steel by wire and arc additive manufacturing, *Int. J. Miner. Metall. Mater.*, 27(2020), No. 7, pp. 933-942. https://doi.org/10.1007/s12613-019-1919-1

Yi-shuang Yu, Bin Hu, Min-liang Gao, Zhen-jia Xie, Xue-quan Rong, Gang Han, Hui Guo, and Cheng-jia Shang, Determining role of heterogeneous microstructure in lowering yield ratio and enhancing impact toughness in high-strength low-alloy steel, *Int. J. Miner. Metall. Mater.*, 28(2021), No. 5, pp. 816-825. https://doi.org/10.1007/s12613-020-2235-5

Xing-hai Yang, Xiao-hua Chen, Shi-wei Pan, Zi-dong Wang, Kai-xuan Chen, Da-yong Li, and Jun-wei Qin, Microstructure and mechanical properties of ultralow carbon high-strength steel weld metals with or without Cu−Nb addition, *Int. J. Miner. Metall. Mater.*, 28(2021), No. 1, pp. 120-130. https://doi.org/10.1007/s12613-020-2159-0

Xiao-feng Wang, Ming-xing Guo, Cun-qiang Ma, Jian-bin Chen, Ji-shan Zhang, and Lin-zhong Zhuang, Effect of particle size distribution on the microstructure, texture, and mechanical properties of Al–Mg–Si–Cu alloy, *Int. J. Miner. Metall. Mater.*, 25(2018), No. 8, pp. 957-966. https://doi.org/10.1007/s12613-018-1645-0

IJMMM WeChat

QQ author group

Effects of heating temperature and atmosphere on element distribution and microstructure in high-Mn/Al austenitic low-density steel

Qi Zhang[1,2], *Guanghui Chen*[1,2,3],✉, *Yuemeng Zhu*[1,2], *Zhengliang Xue*[1,2], *and Guang Xu*[1,2]

1) State Key Laboratory of Refractories and Metallurgy, Wuhan University of Science and Technology, Wuhan 430081, China
2) Key Laboratory for Ferrous Metallurgy and Resources Utilization of Ministry of Education, Wuhan University of Science and Technology, Wuhan 430081, China
3) Zhejiang Red Eagle Group Co., Ltd., Huzhou 313000, China

Abstract: The elemental distribution and microstructure near the surface of high-Mn/Al austenitic low-density steel were investigated after isothermal holding at temperatures of 900–1200°C in different atmospheres, including air, N_2, and $N_2 + CO_2$. No ferrite was formed near the surface of the experimental steel during isothermal holding at 900 and 1000°C in air, while ferrite was formed near the steel surface at holding temperatures of 1100 and 1200°C. The ferrite fraction was larger at 1200°C because more C and Mn diffused to the surface, exuded from the steel, and then reacted with N and O to form oxidation products. The thickness of the compound scale increased owing to the higher diffusion rate at higher temperatures. In addition, after isothermal holding at 1100°C in N_2, the Al content near the surface slightly decreased, while the C and Mn contents did not change. Therefore, no ferrite was formed near the surface. However, the near-surface C and Al contents decreased after holding at 1100°C in the $N_2 + CO_2$ mixed atmosphere, resulting in the formation of a small amount of ferrite. The compound scale was thickest in N_2, followed by the $N_2 + CO_2$ mixed atmosphere, and thinnest in air. Overall, the element loss and ferrite fraction were largest after holding in air at the same temperature. The differences in element loss and ferrite fraction between in N_2 and $N_2 + CO_2$ atmospheres were small, but the compound scale formed in N_2 was significantly thicker. According to these results, $N_2 + CO_2$ is the ideal heating atmosphere for the industrial production of high-Mn/Al austenitic low-density steel.

Keywords: low-density steel; oxidation; microstructure; element distribution; compound scale

1. Introduction

In the 1950s, Fe–Mn–Al–C steels were developed as a substitute for Fe–Cr–Ni stainless steels [1–2]. These steels have garnered significant attention for their potential applications in the automotive industry, owing to their lightweight nature, aligning with the global low-carbon economy and emission reduction requirements [3–4]. Fe–Mn–Al–C low-density steels can be classified into four categories: ferritic steel, ferrite-based duplex steel, austenite-based duplex steel, and austenitic steel [5]. Among these, the austenitic steels show the most promise in terms of performance and processing [6–7]. The tensile properties of austenitic steels subjected to solution treatment are similar to those of high-Mn twinning-induced plasticity (TWIP) steels [6]. The impact toughness of these steels is slightly lower than those of Cr–Ni stainless steels but higher than those of conventional high-strength steels such as quenching & partitioning (Q&P) and transformation-induced plasticity (TRIP) steels [8–9]. Solution treatments are typically conducted at temperatures of 800–1200°C [10]. During solution treatments, decarburization and demanganization result in phase transitions on the steel surface [11–13].

During heat treatment at high temperatures, the steel surface is oxidized by oxidizing gases such as O_2, CO_2, and H_2O [14]. This leads to decarburization reactions, resulting in a reduction in carbon content or even the absence of carbon near the surface [15–18]. Surface decarburization is a common defect in the industrial production of medium- and high-carbon steels, and it can cause various quality problems such as insufficient surface hardness, reduced fatigue life [19], and poor wear resistance [20]. Studies have shown that decarburization is influenced by factors such as heating temperature and time [21], atmosphere [22], and alloying composition [23]. Among these factors, the atmosphere in the heating furnace significantly influences decarburization. The stronger the oxidizing atmosphere, the more intense the decarburization of steel [22]. Therefore, controlling the atmosphere is critical for managing the decarburization reaction on the surface of steel [24].

Manganese (Mn) volatilization usually occurs during the smelting process of Mn steels [25–26]. The Mn volatilization rate increases with temperature and time [27]. Mn volatilization can occur not only during smelting but also during

🍎 Springer

heat treatment [28]. Wild [12] conducted vacuum annealing treatment on Fe–18Cr–9Ni–1.2Mn–0.05C–0.45Mo (concentrations in wt% unless otherwise specified) austenitic stainless steel and observed the escape of Mn from the experimental steel within the temperature range of 497–747°C. Catteau *et al.* [29] performed thermal expansion experiments on Fe–0.4C–1Mn–1Cr–0.25Mo steel in a vacuum and reported that Mn and Cr near the surface evaporated during holding at 875°C for 20 min, which affected the thermal stability of austenite and resulted in microstructural heterogeneities. Kumar and Mahobia [30] reported that Mn atoms diffused from the center to the surface and reacted with O atoms in Fe–8Cr–21Mn–0.65C austenitic stainless steel while holding at 500–700°C, leading to a less stable austenite.

Studies have investigated the effects of decarburization or demanganization during high-temperature heat treatment. However, the elemental distributions near the surface and their impacts on microstructure evolution have not been quantitatively and systematically analyzed. Additionally, the loss of elements during heat treatment may vary with the atmosphere. However, studies have not compared the effects of different atmospheres on decarburization and demanganization. Therefore, the present study investigates the elemental distribution and microstructural evolution in high-Mn/Al austenitic low-density steel after heat treatment at high temperatures in three atmospheres: air, N_2, and $CO_2 + N_2$. The goal of this study is to provide theoretical guidance for controlling the surface quality of high-Mn/Al austenitic low-density steel in industrial production.

2. Experimental

The austenitic low-density steel with the chemical composition of Fe–20Mn–6Al–0.6C–0.15Si was melted and cast in a 50 kg-vacuum induction furnace and then cooled to room temperature. The ingots were reheated to 1250°C and held for 2 h for homogenization. The ingots were then forged into round bars with a diameter of 60 mm, followed by cooling to room temperature in a furnace. The starting and finishing forging temperatures were 1100 and 950°C, respectively. To study the influence of temperature on the element distribution and microstructure, the experimental steel was heated to 900–1200°C and isothermally held for 1 h, followed by quenching to room temperature. The heat treatments were performed in air. To compare the impact of the atmosphere, the steel was isothermally held at 1100°C in 100%N_2 and 75%N_2 + 25%CO_2 (All gas percentages below are volume fractions). N_2 is usually used as a protective gas. The mixed atmosphere of 75%N_2 + 25%CO_2 was used to simulate the atmosphere after full combustion of the blast furnace gas in air, which consists of 72%N_2, 23%CO_2, and 5%H_2O(g). Considering the small proportion of H_2O(g), the atmosphere was set to 75%N_2 + 25%CO_2 to simulate the atmosphere in the heating furnace.

The microstructure of as-forged steel was observed via electron channeling contrast imaging (ECCI) and electron

backscatter diffraction (EBSD) on an Apreo S HiVac field-emission scanning electron microscope. The initial microstructure was analyzed using a SmartLab SE X-ray diffractometer with Cu K_α radiation. Additionally, the microstructure beneath the compound scale of the specimen held at 1200°C in air was analyzed via X-ray diffraction (XRD) after the grinding and polishing of the compound scale. After heat treatment, the microstructure of the cross section was mechanically ground and polished for microstructure analyses via scanning electron microscopy (SEM) and EBSD. The distribution of elements near the surface was quantitatively analyzed using an EPMA-8050G field-emission electron probe microanalyzer equipped with wavelength dispersive spectrometers. The equilibrium phase diagrams were calculated using Thermo-Calc 2023b. The adopted database was TCFE 12: Steels/Fe-Alloys v12.0.

3. Results and discussion

3.1. Effect of temperature in air

The ECCI micrograph and XRD pattern of the initial microstructure of the experimental steel (Fig. 1(a) and (b)) indicated that the initial microstructure was fully austenitic. However, after heat treatment at 1200°C for 1 h in air, ferrite occurred near the surface, as shown in the EBSD phase map (Fig. 1(c)). The XRD pattern (Fig. 1(d)) further confirmed the presence of significant ferrite under the oxidized layer of the specimen. This unexpected ferrite formation is attributable to the reduced stability of austenite, which was caused by the loss of alloying elements during heat treatment [31–33]. The fraction of ferrite was influenced by several factors, including isothermal temperature, isothermal time, and atmosphere.

To further investigate the impact of isothermal temperature on the ferrite fraction, the experimental steel was isothermally held at temperatures of 900–1200°C for 1 h in air, and their microstructure was analyzed via EBSD. The micrographs are shown in Fig. 2. After isothermal holding at 900°C and 1000°C, the microstructure remained fully austenitic (Fig. 2(a)). Different fractions of ferrite were formed near the surface after isothermal holding at 1100 and 1200°C (Fig. 2(b)–(d)).

For each condition, the ferrite occurrence depth was measured according to five micrographs (Fig. 3(a)). The ferrite farthest from the surface was used as a standard point. A rectangle region (dashed line) was obtained by drawing a line parallel to the surface from the standard point (Fig. 2). The area of the rectangle was measured and recorded as *S*. The area of the ferrite region (S_1) was determined using Image-Pro Plus software. The ratio of S_1 to *S* represents the area fraction of ferrite, which can be considered the volume fraction of ferrite near the surface. The fractions of ferrite after heat treatment at different temperatures are plotted in Fig. 3(b). Both the ferrite occurrence depth and the ferrite fraction significantly increased with increasing holding temperature.

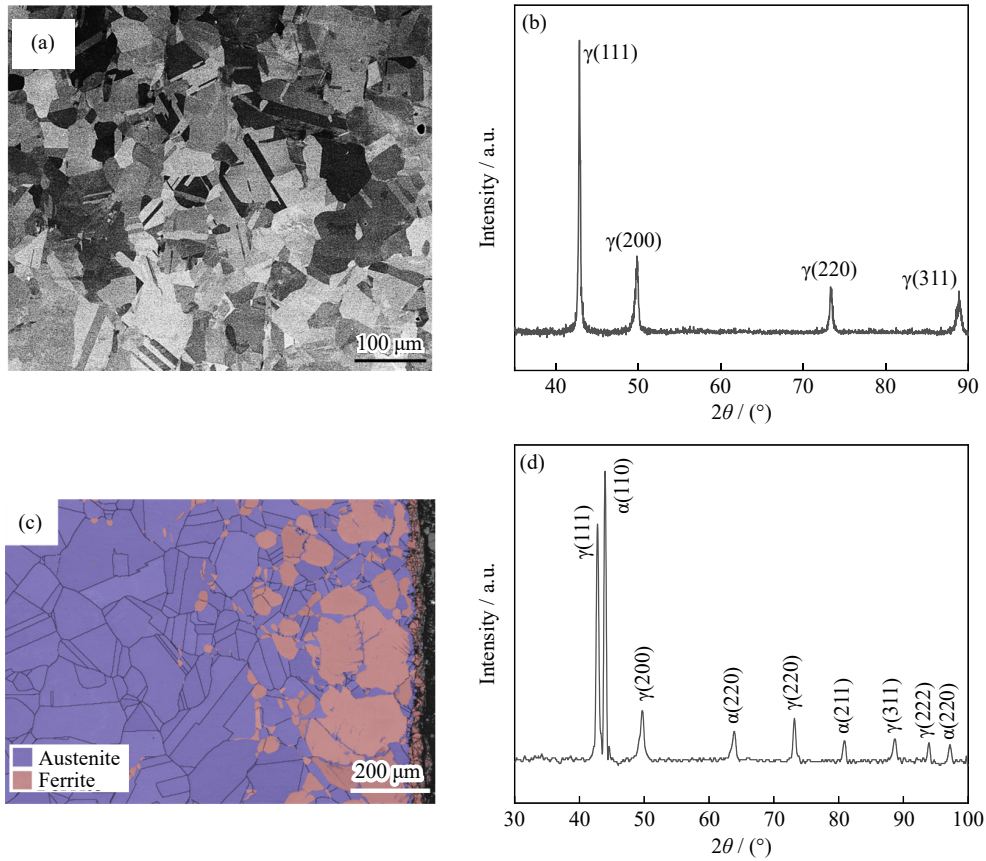The distributions of C, Mn, and Al near the surface after

Fig. 1. (a) ECCI micrograph and (b) XRD pattern of the initial microstructure; (c) EBSD phase map of the microstructure after isothermal holding at 1200°C for 1 h in air; (d) XRD analysis of the microstructure with a removal of the surface compound scale after isothermal holding at 1200°C.
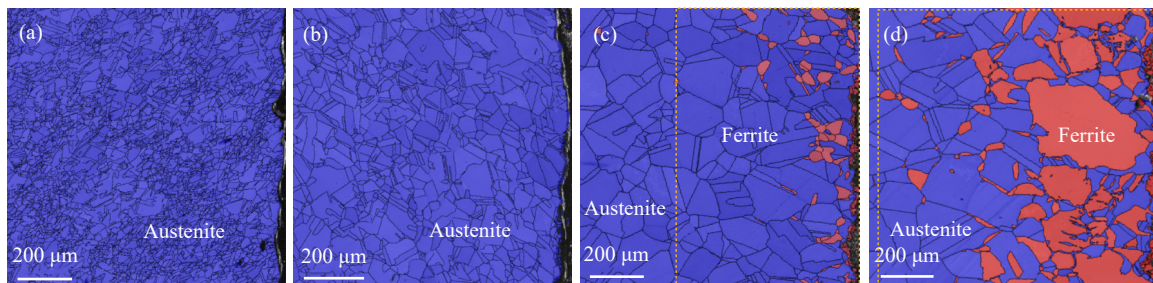

Fig. 2. EBSD analyses of samples after isothermal holding at different temperatures for 1 h in air: (a) 900°C; (b) 1000°C; (c) 1100°C; (d) 1200°C. Ferrite is highlighted in orange.
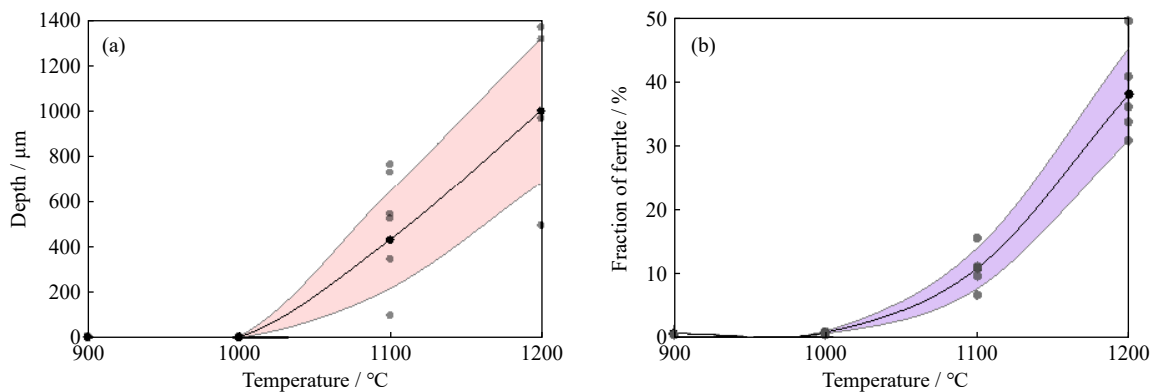

Fig. 3. (a) Ferrite occurrence depth and (b) ferrite fraction of sample after isothermal holding at 900–1200°C in air. The shadow represents the standard deviation.

heat treatment were quantitatively analyzed through electron probe microanalysis (EPMA)–wavelength dispersive spec-

trometry (WDS) line scanning (Fig. 4). The C, Al, and Mn contents significantly fluctuated, attributable to the ferritic
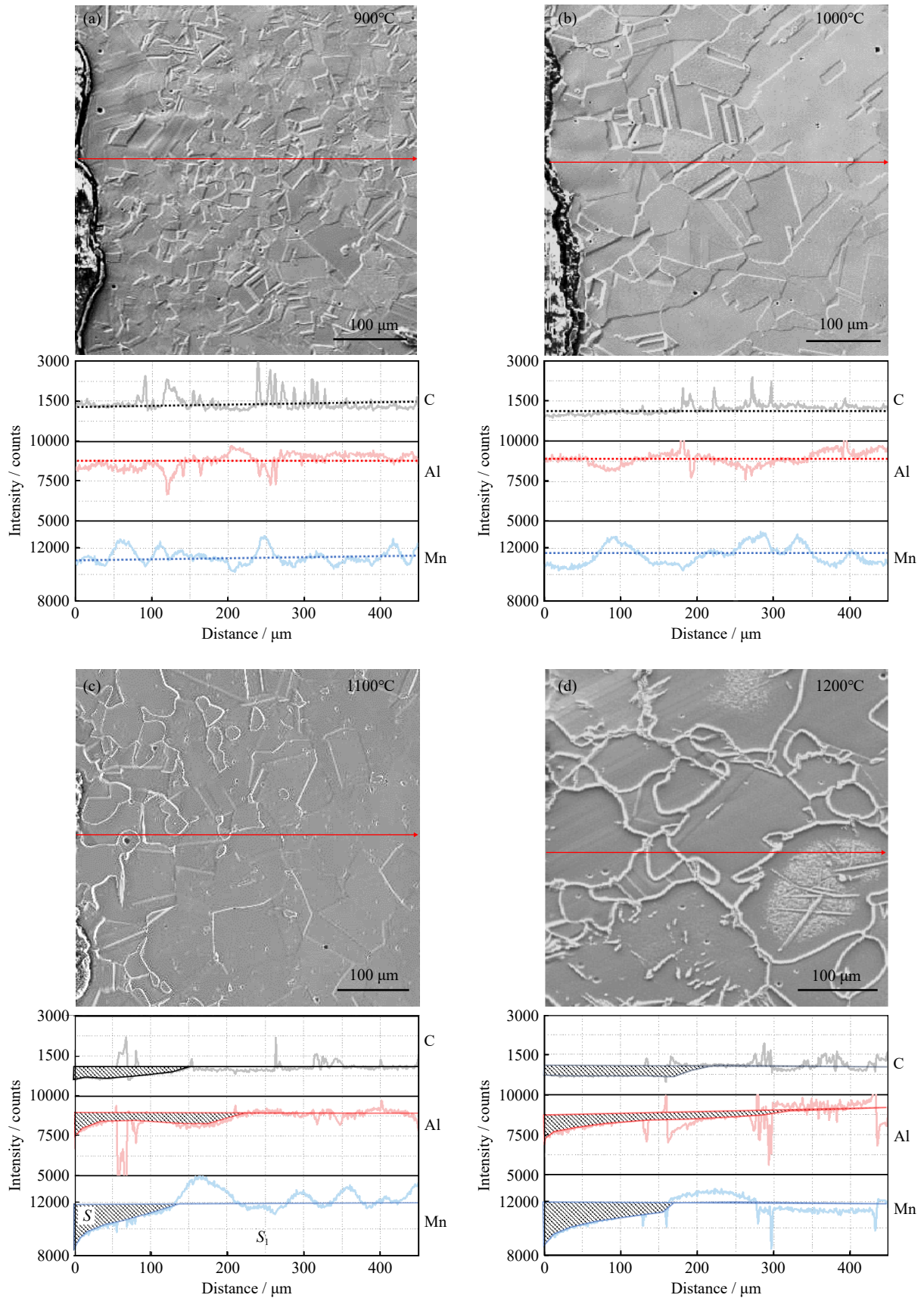

Fig. 4. SEM micrographs and corresponding EPMA–WDS line scanning results after heat treatments at different temperatures in air: (a) 900°C; (b) 1000°C; (c) 1100°C; (d) 1200°C.

solidification mode of the experimental steel. During solidification, the liquid first transformed into δ-ferrite. At high temperatures, alloying elements such as C, Mn, and Al were rapidly partitioned between the liquid and δ-ferrite phases, leading to significant differences in alloying content. Subsequently, both the liquid and δ-ferrite transformed into austenite during the cooling process. According to Fig. 5(a), the newly formed austenite inherited the alloying elements from the parent liquid and δ-ferrite, thereby resulting in local segregation. The fluctuations in C, Mn, and Al contents are attributable to the local segregation of elements during peritectic solidification, despite the experimental steel under-

going thermomechanical treatments such as forging and homogenization (1250°C for 2 h) [34–36]. To confirm this possibility, additional EPMA–WDS analysis was conducted to investigate the element distribution in a region away from the specimen surface (Fig. 5(b)), where no element loss occurred during the heating treatment. However, the Mn content largely fluctuated (Fig. 5(c)). Therefore, the fluctuation in alloying elements is attributable to the local segregation induced by peritectic solidification. Additionally, alloying elements tend to accumulate at grain boundaries [37]. This also possibly contributed to the fluctuation in element contents.
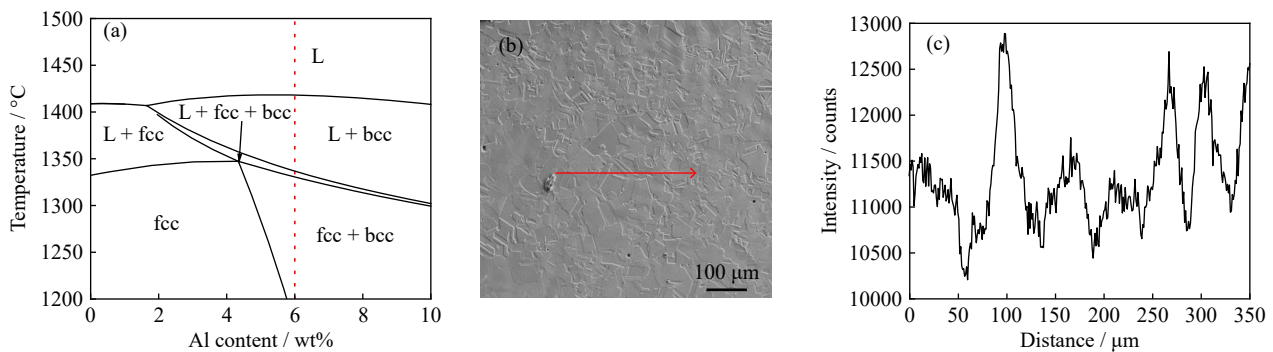

Fig. 5. (a) Equilibrium phase diagrams; (b) EPMA–WDS analysis region away from the surface of the specimen held at 900°C in air; (c) distribution of Mn intensity. L: liquid; bcc: body centred cube; fcc: face centre cube.

The concentrations of alloying elements almost remained relatively constant at the isothermal holding temperatures of 900 and 1000°C (Fig. 4(a) and (b)). The fluctuation was likely due to peritectic segregation and grain boundary segregation. However, at higher holding temperatures of 1100 and 1200°C, the Al and Mn contents notably decreased, with a slight decrease in the C content near the surface, disregarding segregation and element partition between ferrite and austenite. According to the EPMA–WDS line scanning results, the percentage of element loss can be approximately using Eq. (1):

$$P = S / (S + S_1) \times 100\% \tag{1}$$

where P represents the percentage of element loss, and S and S_1 are the areas of the corresponding regions illustrated in Fig. 4(d). The estimation results (Fig. 6) indicate that the loss of Mn, C, and Al near the surface became more pronounced at higher temperatures.

Mn, C, and Al atoms diffused to the surface and reacted with the gas in the environment, resulting in a reduction in the Mn, C, and Al contents near the surface. The loss of alloying elements is primarily influenced by their initial contents and diffusion rates [12,28−29]. Fig. 7 shows the diffusion rates of Mn, C, and Al in austenitic lattice simulated using Thermo-Calc software. As the temperature increased, the diffusion rates of the elements also increased, leading to a more significant exudation of Mn, C, and Al at higher temperatures.

According to Huang *et al.* [38], Al, as the primary oxygen-getter, underwent initial oxidation to form a loose Al_2O_3 film, which facilitated the diffusion of Mn and C atoms. Owing to

the high content of Mn (20wt%) in the experimental steel, the relative percentage of Mn loss was significantly higher than those of Al and C. However, the diffusion rate of C was much higher than those of Mn and Al, which contradicts the observation that C loss was the smallest (Fig. 7). Duh and Wang [39] reported that decarburization played a major role in the initial oxidation stage in Fe–30Mn–9Al–0.87C low-density steel. However, as oxidation progressed, it was primarily controlled by metal elements such as Mn and Al once decarburization reached a steady state. As a result, the losses of Mn and Al were larger than that of C.

The exudation of C and Mn, commonly accepted as austenite stabilizers, resulted in a decrease in the thermal stability of austenite near the surface. The depletion of C and Mn
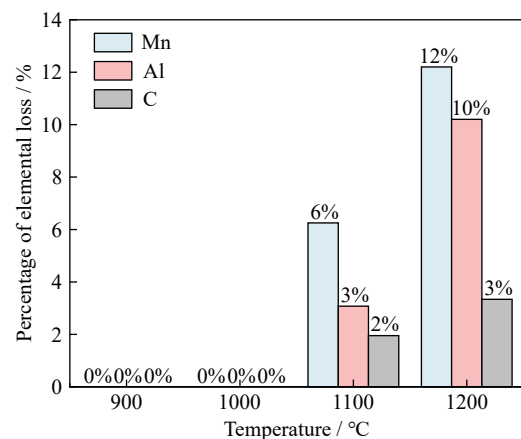

Fig. 6. Percentages of Mn, C, and Al loss after isothermal holding at different temperatures in air.
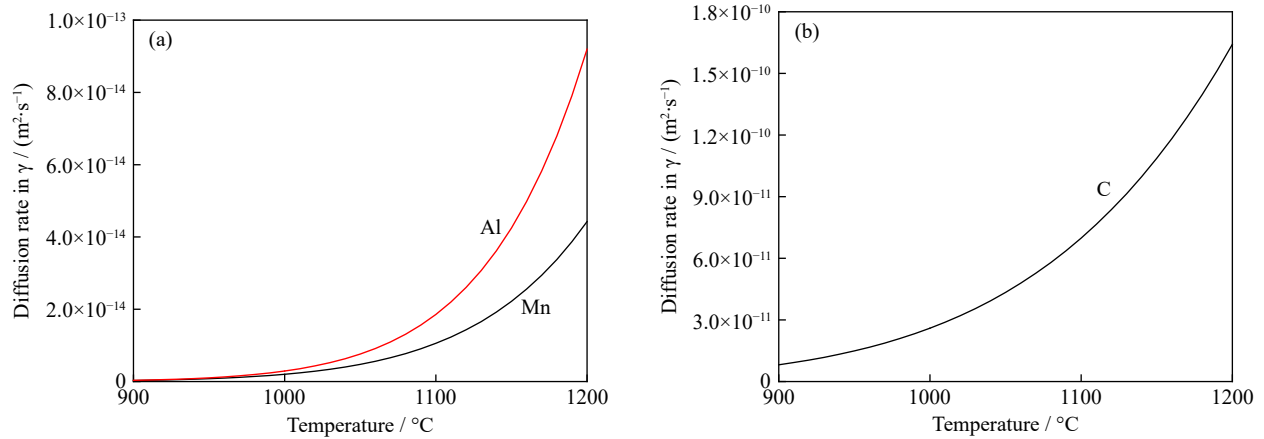
Fig. 7. Diffusion rates of (a) Mn/Al and (b) C, as simulated using Thermo-Calc software.

may explain the presence of ferrite near the surface after isothermal holding at high temperatures. The Thermo-Calc equilibrium phase diagrams (Fig. 8) indicated that the ferrite fraction increased with the decrease in the Mn and C contents. Therefore, the decrease in Mn and C contents near the surface, which became more pronounced at higher temperatures, explains the formation of ferrite near the surface, with additional ferrite forming after isothermal holding at higher temperatures (Fig. 3). Despite the loss of some Al at the surface, which would normally inhibits ferritic transformation (Fig. 8(c)), ferrite was still formed. Additionally, Si was possibly lost during heating treatments. The effect of the Si content on the transformation of the experimental steel is illustrated in Fig. 8(d). The variation in the Si content had little influence on the transformation. However, Si combined with O and Fe during heating treatment and formed oxidation products such as SiO_2 and Fe_2SiO_4 [40]. Given the low Si content and its minimal impact, the effect of Si loss on the transformation and compound scale can be disregarded.

After oxidization, a compound scale layer occurred on the surface of the experimental steel (Fig. 9(a)–(d)). The mean thickness of this scale was estimated and plotted (Fig. 9(e)). Fig. 9(e) shows an increase in thickness with increasing isothermal temperature. The composition of the compound scale after holding at 1100°C was analyzed via EPMA–WDS line scanning (Fig. 10). The compound scale primarily consisted
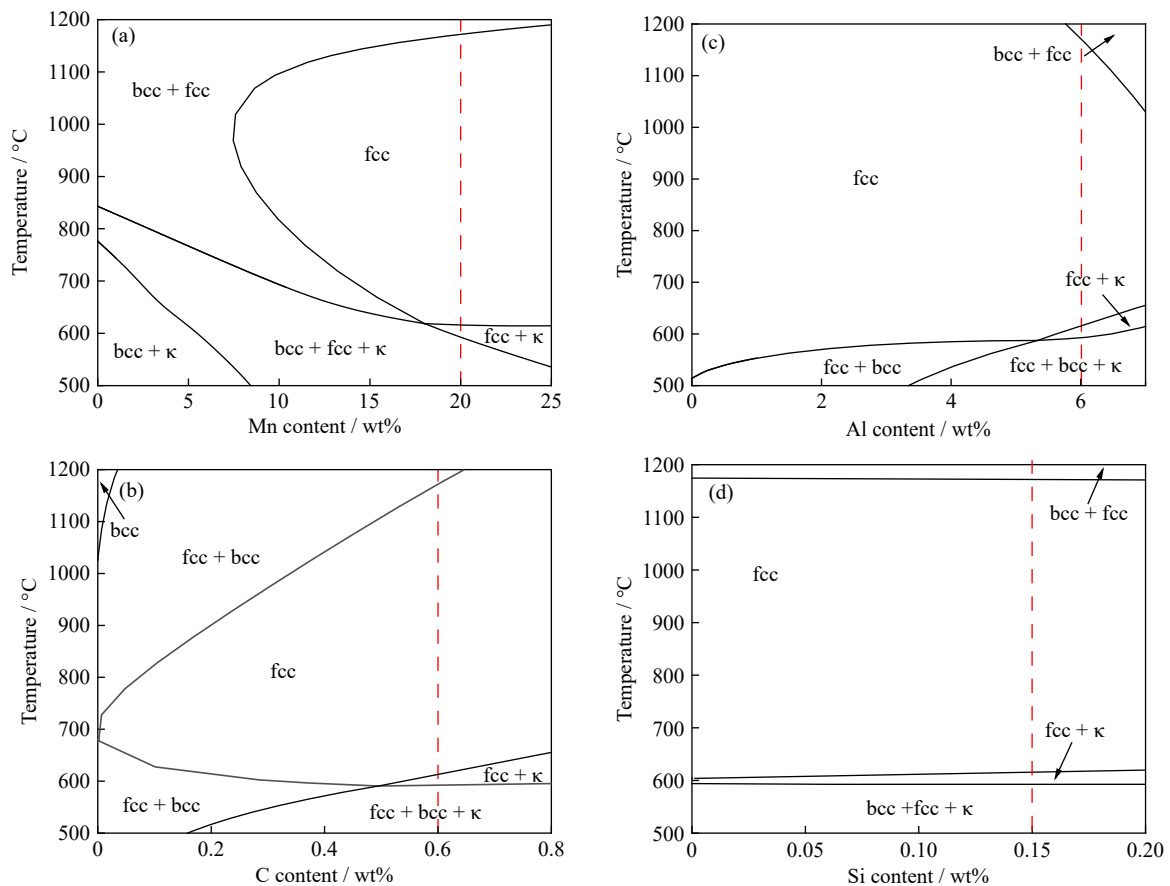

Fig. 8. Equilibrium phase diagrams corresponding to different Mn (a), C (b), Al (c), and Si (d) contents.
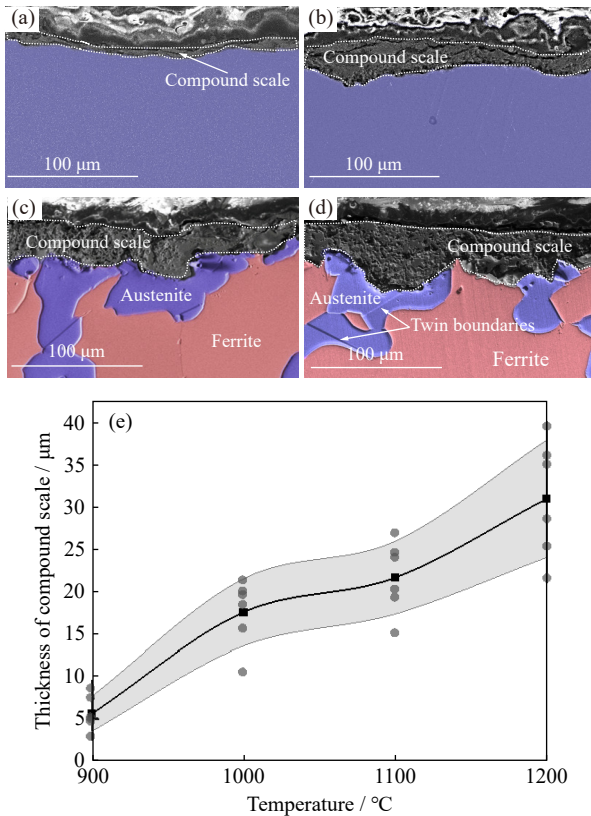
Fig. 9. **SEM micrographs of the compound scale after isothermal holding at different temperatures in air: (a) 900°C; (b) 1000°C; (c) 1100°C; (d) 1200°C. (e) Thickness of the compound scale as a function of temperature. The shadow in (e) represents the standard deviation.**

of chemical components originating from the experimental steel, including C, Al, Mn, and Fe, along with N and O from the atmosphere. According to the literatures [38–39,41], the compound scale of Fe–Mn–Al–C steels likely contained Mn_2O_3, Fe_2O_3, Mn_3O_4, $MnFe_2O_4$, $(Mn,Fe)O$, and $MnAl_2O_4$. During the initial oxidation stages, Al was the first element to be oxidized, forming discontinuous Al_2O_3 structures [42]. This allowed for the infiltration of N_2 and O_2 into the matrix. AlN may form before the oxidation by O_2 because the formation rate of Al_2O_3 was low, and N_2 could easily permeate into the matrix [43]. Other elements, such as C, Mn, and Fe, reacted with O_2 to form oxidation products [44]. Additionally,

at higher temperatures, the diffusion rate increased, allowing for more alloying elements to reach the surface and undergo oxidation. This explains the thicker compound scale at higher temperatures.

3.2. Effect of atmosphere at 1100°C

Fig. 11 presents the EBSD analysis near the surface after isothermal holding at 1100°C in N_2 and $N_2 + CO_2$. As discussed earlier, the formation of ferrite after holding in air (Fig. 2(c)) was due to the exudation of Mn and C. The near-surface microstructure (Fig. 11(a)) indicated the absence of ferrite after isothermal holding in N_2. However, a small amount of ferrite was formed near the surface of the experimental steel after holding in a $N_2 + CO_2$ atmosphere (Fig. 11(b)). The depth and fraction of ferrite in different atmospheres are plotted in Fig. 12. The degree of ferritic transformation after isothermal holding was highest in air but lowest in the N_2 atmosphere.

The distributions of C, Al, and Mn near the surface of the samples treated in N_2 and in $N_2 + CO_2$ were analyzed via EPMA–WDS line scanning (Fig. 13). Similar to the samples treated in air (Fig. 4(c)), the contents of alloying elements C, Mn, and Al in the samples treated in N_2 still fluctuated. As explained in Section 3.1, the fluctuations in element content were caused by local segregation due to peritectic solidification and accumulation at grain boundaries. These fluctuations were not affected by the heating atmosphere. The samples treated in air exhibited a decrease in the C, Mn, and Al contents near the surface (Fig. 4(c)). However, for the sample treated in N_2, the C, Mn, and Al contents near the surface were similar to those at the inner part (Fig. 13(a)). Accordingly, ferrite was absent from the surface after holding in N_2. Only a small amount of ferrite was formed near the surface after isothermal holding in the $N_2 + CO_2$ mixed atmosphere (Fig. 13(b)). The ferrite fraction was significantly less than that in the specimen treated in air. According to the EPMA–WDS line scanning results (Fig. 13(b)), the C content decreased near the surface. This indicates that decarburization occurred on the surface during isothermal holding in $N_2 + CO_2$, but no demanganization reaction was observed. According to the EPMA–WDS line scanning results for the specimens subjected to isothermal holding in different atmo-
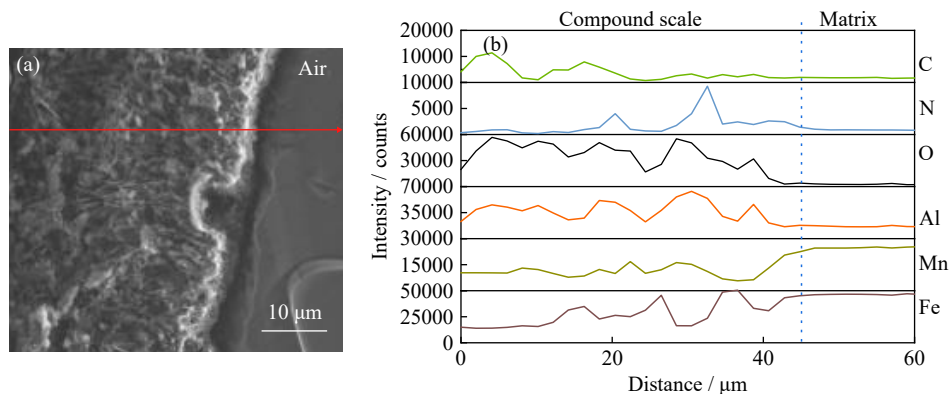

Fig. 10. **EPMA–WDS line scanning results for the compound scale after isothermal holding at 1100°C in air: (a) micrograph of compound scale and matrix; (b) EPMA–WDS line scanning results.**
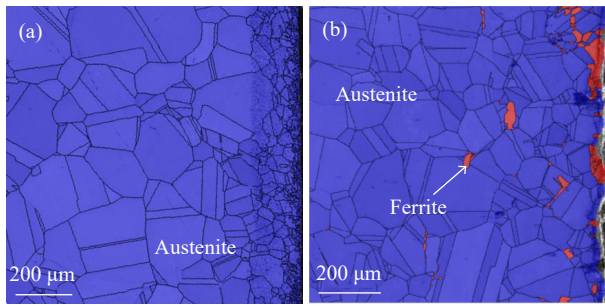
Fig. 11.   EBSD analysis after isothermal holding at 1100°C in different atmospheres: (a) N_2; (b) $N_2 + CO_2$. Ferrite is highlighted in orange.

spheres (Figs. 4(c) and 13), the degree of decarburization reaction in different atmospheres was in the following order: air > $N_2 + CO_2$ > N_2, and the demanganization degree was in the order: air > N_2 = $N_2 + CO_2$.

The ferritic transformation degree after isothermal holding in air, N_2, and $N_2 + CO_2$ was in the following order: air >

$N_2 + CO_2 > N_2$. This trend was due to the simultaneous occurrence of decarburization and demanganization, which resulted in isothermal holding in air, yielding the highest degree of ferritic transformation. Only considerable decarburization occurred during holding in $N_2 + CO_2$; therefore, the ferritic transformation degree was lower than that in air. Additionally, no ferrite was formed during isothermal holding in N_2, as neither decarburization nor demanganization reactions occurred.

After the samples were held at a constant temperature in N_2 or $N_2 + CO_2$ mixed atmosphere, the compound scales were more likely to have a uniform thickness compared with those formed in air. The thickness of the compound scale formed in air was ~24 μm, while the thickness of that formed in N_2 reached 144 μm. With heat treatment in $N_2 + CO_2$, the estimated thickness was ~93 μm. Fig. 14 shows the SEM micrographs and corresponding EPMA–WDS line scanning results of compound scales after isothermal holding in N_2, and $N_2 + CO_2$ atmospheres.
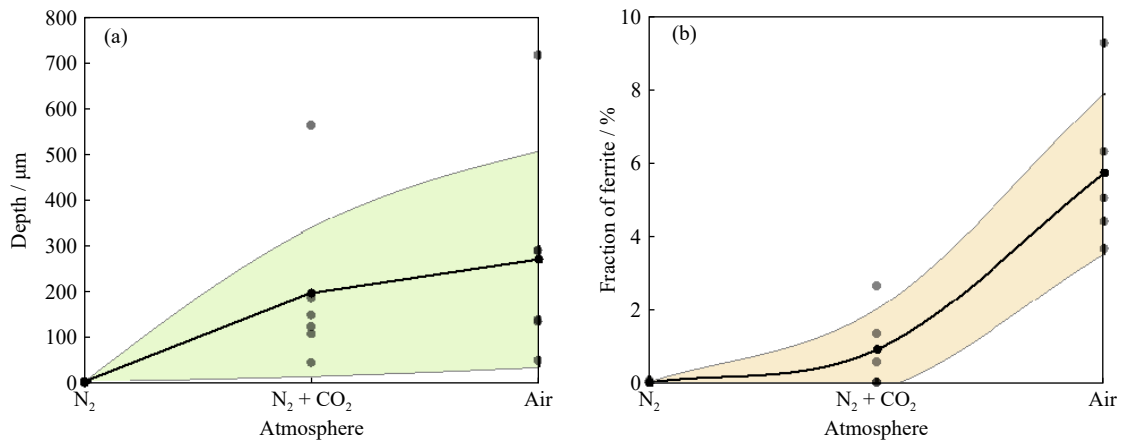

Fig. 12.   (a) Ferrite occurrence depth and (b) fraction of ferrite of samples after isothermal holding at different atmospheres. The shadow represents the standard deviation.
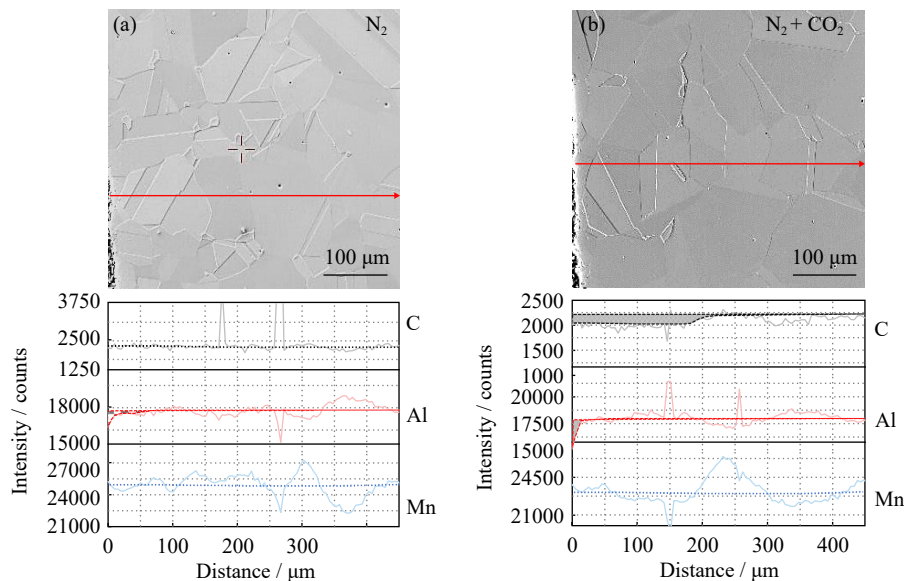

Fig. 13.   SEM micrographs of the matrix and corresponding EPMA–WDS line scanning results after isothermal holding at 1100°C for 1 h in different atmospheres: (a) N_2; (b) $N_2 + CO_2$.
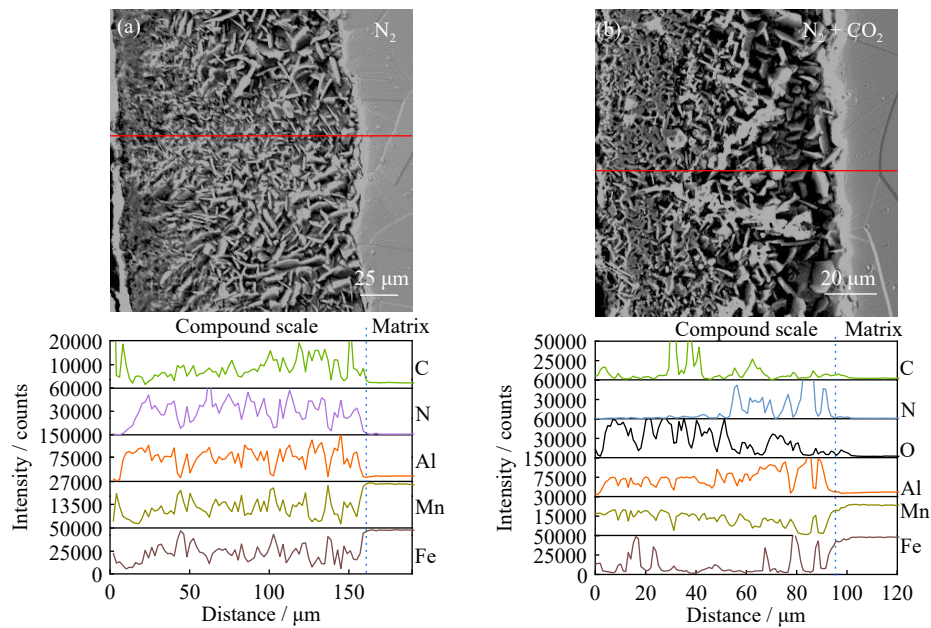
Fig. 14.   SEM micrographs of the compound scale and corresponding WDS line scanning results after isothermal holding at 1100°C in (a) N_2; (b) $N_2 + CO_2$.

As discussed previously, during isothermal holding in air, (Fig. 10) the alloying elements such as Mn, Al, and Fe reacted with N_2 and O_2 to form products of oxidation. During isothermal holding in N_2, nitrogen easily dissolved into the matrix and formed lamellar AlN (Fig. 14(a)). This phenomenon is similar to the findings of Park *et al*. [41]. In addition, according to morphology analysis and the EPMA–WDS line scanning results (Fig. 14(b)), the compound scale formed in the $N_2 + CO_2$ atmosphere consisted of two layers. The inner layer was mainly composed of nitrides such as AlN and the outer layer contained oxides (M_xO_y). Initially, Al reacted with N to form AlN [43], and then some AlN was oxidized by CO_2. Other alloying elements in the matrix, such as Fe, Mn, and C, were also oxidized by CO_2 to form corresponding oxidation products. The formation of AlN explains the slight reduction in Al content near the surface (Fig. 13(a) and (b)).

The compound scale formed in N_2 was the thickest, while the loss of Al was not very significant. The loss of elements mainly depended on the oxidation properties of the atmosphere rather than the thickness of the compound scale. Air exhibited the strongest oxidation capability owing to the presence of O_2. CO_2 had a weaker oxidation capability. The oxidation capability of N_2 was weaker than those of O_2 and CO_2. Therefore, air had the strongest oxidation capability, while N_2 had the weakest. The oxidation capability of $N_2 + CO_2$ mixed atmosphere was intermediate. Consequently, the dealuminification degree was as follows: air >> $N_2 + CO_2$ > N_2. Moreover, the compound scale formed in N_2 was AlN, with a density of only 3.26 g/cm³. The oxidation products formed in air and $N_2 + CO_2$ consisted of AlN and oxides of Fe, Mn, and Al. Among these, AlN had the lowest density, which explains the formation of a thicker compound scale in N_2.

4. Conclusions

The austenitic low-density steel with the composition of Fe–20Mn–6Al–0.6C–0.15Si was isothermally held at temperatures ranging from 900 to 1200°C in air, N_2, and $N_2 + CO_2$ atmospheres. The elemental distribution and microstructure near the surface were analyzed via SEM, XRD, EBSD, and EPMA. The following conclusions can be drawn.

(1) No ferrite was formed near the surface of the experimental steel during isothermal holding at 900°C and 1000°C in air. However, when the isothermal temperature reached 1100°C, some ferrite was formed near the surface, and more ferrite was formed as the temperature was further increased to 1200°C. This is attributed to the exudation of austenite stabilizers C and Mn during holding at higher temperatures.

(2) During isothermal holding in air, the alloying elements diffused to the surface and reacted with N and O from the air, forming products of oxidation on the surface. The thickness of the compound scale increased with the isothermal temperature owing to the increased diffusion rate of the alloying elements.

(3) After isothermal holding at 1100°C in N_2, the near-surface Al content slightly decreased, while the C and Mn contents remained unchanged. Therefore, no ferrite was formed near the surface. However, after holding in the $N_2 + CO_2$ mixed atmosphere, the C and Al contents near the surface decreased, leading to the formation of a small amount of ferrite.

(4) A comparison of isothermal holding in the three atmospheres at the same temperature revealed that holding in air yielded both the highest element loss and ferrite fraction. The differences in element loss and ferrite fraction between N_2 and $N_2 + CO_2$ mixed atmospheres were small, but the compound scale formed in $N_2 + CO_2$ was much thinner. Therefore, $N_2 + CO_2$ is the ideal heating atmosphere for the industrial production of high-Mn/Al austenitic low-density steel.

Acknowledgements

Conflict of Interest

All authors state that there is no conflict of interest.

References

[1] S.F. Hu, Z.B. Zheng, W.P. Yang, and H.K. Yang, Fe–Mn–C–Al low-density steel for structural materials: A review of alloying, heat treatment, microstructure, and mechanical properties, *Steel Res. Int.*, 93(2022), No. 9, art. No. 2200191.

[2] H. Ding, D.G. Liu, M.H. Cai, and Y. Zhang, Austenite-based Fe–Mn–Al–C lightweight steels: Research and prospective, *Metals*, 12(2022), No. 10, art. No. 1572.

[3] C.M. Tang, Z.Q. Guo, J. Pan, *et al.*, Current situation of carbon emissions and countermeasures in China's ironmaking industry, *Int. J. Miner. Metall. Mater.*, 30(2023), No. 9, p. 1633.

[4] X. Lu, W.J. Tian, H. Li, X.J. Li, K. Quan, and H. Bai, Decarbonization options of the iron and steelmaking industry based on a three-dimensional analysis, *Int. J. Miner. Metall. Mater.*, 30(2023), No. 2, p. 388.

[5] I. Gutierrez-Urrutia, Low density Fe–Mn–Al–C steels: Phase structures, mechanisms and properties, *ISIJ Int.*, 61(2021), No. 1, p. 16.

[6] S.P. Chen, R. Rana, A. Haldar, and R.K. Ray, Current state of Fe–Mn–Al–C low density steels, *Prog. Mater. Sci.*, 89(2017), p. 345.

[7] H.T. Lu, D.Z. Li, S.Y. Li, and Y.A. Chen, Hot deformation behavior of Fe–27.34Mn–8.63Al–1.03C lightweight steel, *Int. J. Miner. Metall. Mater.*, 30(2023), No. 4, p. 734.

[8] N.I. Ramos-Fabián, I. Mejía, M. García-Domínguez, and A. Bedolla-Jacuinde, Metallographic, structural and mechanical characterization of a low-density austenitic Fe–Mn–Al–C steel microalloyed with Nb in hot-rolling condition, *MRS Adv.*, 8(2023), No. 22, p. 1291.

[9] Y.X. Liu, M.X. Liu, J.L. Zhang, *et al.*, Microstructure and mechanical properties of a Fe–28Mn–9Al–1.2C–(0, 3, 6, 9)Cr austenitic low-density steel, *Mater. Sci. Eng. A*, 821(2021), art. No. 141583.

[10] K.T. Park, S.W. Hwang, C.Y. Son, and J.K. Lee, Effects of heat treatment on microstructure and tensile properties of a Fe–27Mn–12Al–0.8C low-density steel, *JOM*, 66(2014), No. 9, p. 1828.

[11] S. Li, Z.N. Yang, H.S. Zurob, H. Chen, C. Zhang, and Z.G. Yang, On the decarburization of surface pearlite, *Metall. Mater. Trans. A*, 52(2021), No. 8, p. 3198.

[12] R.K. Wild, Vacuum annealing of stainless steel at temperatures between 770 and 1470K, *Corros. Sci.*, 14(1974), No. 10, p. 575.

[13] Q. Zhang, G.H. Chen, Y.P. Shen, Z.L. Xue, and G. Xu, Microstructure evolution on the surface of Fe–20Mn–6Al–0.6C–0.15Si austenitic low-density steel during heat treatment, *J. Mater. Eng. Perform.*, (2023). DOI: 10.1007/s11665-023-08803-7

[14] M.X. Zhou, H.X. Wang, M. Zhu, *et al.*, New insights to the metallurgical mechanism of niobium in high-carbon pearlitic steels, *J. Mater. Res. Technol.*, 26(2023), p. 1609.

[15] H.D. Alvarenga, T. van de Putte, N. van Steenberge, J. Sietsma,

and H. Terryn, Influence of carbide morphology and microstructure on the kinetics of superficial decarburization of C–Mn steels, *Metall. Mater. Trans. A*, 46(2015), No. 1, p. 123.

[16] Y. Guo, F.Q. Dai, S.T. Hu, and G. Xu, Effect of surface oxidation on decarburization of a Fe–3%Si steel during annealing, *ISIJ Int.*, 58(2018), No. 9, p. 1727.

[17] M. Hajduga and J. Kučera, Decarburization of Fe–Cr–C steels during high-temperature oxidation, *Oxid. Met.*, 29(1988), No. 5, p. 419.

[18] X.N. Duan, H. Yu, J. Lu, and Z. Huang, Temperature dependence and formation mechanism of surface decarburization behavior in 35CrMo steel, *Steel Res. Int.*, 90(2019), No. 9, art. No. 1900188.

[19] M.J. Gildersleeve, Relationship between decarburisation and fatigue strength of through hardened and carburising steels, *Mater. Sci. Technol.*, 7(1991), No. 4, p. 307.

[20] R.I. Carroll and J.H. Beynon, Decarburisation and rolling contact fatigue of a rail steel, *Wear*, 260(2006), No. 4-5, p. 523.

[21] A. Rafiei, G.A. Irons, and K.S. Coley, Argon-oxygen decarburization of high manganese steels: Effect of temperature, alloy composition, and submergence depth, *Metall. Mater. Trans. B*, 52(2021), No. 4, p. 2509.

[22] Y.R. Chen, X.X. Xu, and Y. Liu, Decarburization of 60Si$_2$MnA in atmospheres containing different levels of oxygen, water vapour and carbon dioxide at 700–1000°C, *Oxid. Met.*, 93(2020), No. 1, p. 105.

[23] Y.B. Liu, W. Zhang, Q. Tong, and Q.S. Sun, Effects of Si and Cr on complete decarburization behavior of high carbon steels in atmosphere of 2 vol.% O$_2$, *J. Iron Steel Res. Int.*, 23(2016), No. 12, p. 1316.

[24] M. Nomura, H. Morimoto, and M. Toyama, Calculation of ferrite decarburizing depth, considering chemical composition of steel and heating condition, *ISIJ Int.*, 40(2000), No. 6, p. 619.

[25] J.H. Chu and Y.P. Bao, Mn evaporation and denitrification behaviors of molten Mn steel in the vacuum refining with slag process, *Int. J. Miner. Metall. Mater.*, 28(2021), No. 8, p. 1288.

[26] J.H. Chu and Y.P. Bao, Volatilization behavior of manganese from molten steel with different alloying methods in vacuum, *Metals*, 10(2020), No. 10, art. No. 1348.

[27] F.J. Lan, C.L. Zhuang, C.R. Li, J.B. Chen, G.K. Yang, and H.J. Yao, Study on manganese volatilization behavior of Fe–Mn–C–Al twinning-induced plasticity steel, *High Temp. Mater. Process.*, 40(2021), No. 1, p. 461.

[28] A.F. Smitll and R. Hales, Diffusion of manganese in type 316 austenitic stainless steel, *Met. Sci.*, 9(1975), No. 1, p. 181.

[29] S.D. Catteau, T. Sourmail, and A. Moine, Dilatometric study of phase transformations in steels: Some issues, *Mater. Perform. Charact.*, 5(2016), No. 5, p. 564.

[30] S. Kumar and G.S. Mahobia, Cyclic oxidation of Fe–18Cr–21Mn–0.65N austenitic stainless steel at 400–700°C, *Trans. Indian Inst. Met.*, 73(2020), No. 10, p. 2457.

[31] Y. Guo, J.H. Zhao, B. Xu, C. Gu, K.Q. Feng, and Y.J. Wang, Effect of high-temperature oxidation on the subsurface microstructure and magnetic property of medium manganese austenitic steel, *J. Alloys Compd.*, 913(2022), art. No. 165254.

[32] V. de Freitas Cunha Lins, M.A. Freitas, and E.M. de Paula E Silva, Oxidation kinetics of an Fe–31.8Mn–6.09Al–1.60Si–0.40C alloy at temperatures from 600 to 900°C, *Corros. Sci.*, 46(2004), No. 8, p. 1895.

[33] A.M. de Sousa Malafaia, L. Latu-Romain, and Y. Wouters, High temperature oxidation resistance improvement in an FeMnSiCrNi alloy by Mn-depletion under vacuum annealing, *Mater. Lett.*, 241(2019), p. 164.

[34] G.H. Chen, R. Rahimi, G. Xu, H. Biermann, and J. Mola, Impact of Al addition on deformation behavior of Fe–Cr–Ni–Mn–C austenitic stainless steel, *Mater. Sci. Eng. A*, 797(2020), art. No. 140084.

[35] G.H. Chen, G. Xu, H. Biermann, and J. Mola, Microstructure and mechanical properties of Co-added and Al-added austenitic stainless steels, *Mater. Sci. Eng. A*, 854(2022), art. No. 143832.

[36] P. Han, Z.P. Liu, Z.J. Xie, *et al.*, Influence of band microstructure on carbide precipitation behavior and toughness of 1 GPa-grade ultra-heavy gauge low-alloy steel, *Int. J. Miner. Metall. Mater.*, 30(2023), No. 7, p. 1329.

[37] A.J. Maldonado, K.P. Misra, and R.D.K. Misra, Grain boundary segregation in a high entropy alloy, *Mater. Technol.*, 38(2023), No. 1, art. No. 2221959.

[38] Z.Y. Huang, Y.S. Jiang, A.L. Hou, *et al.*, Rietveld refinement, microstructure and high-temperature oxidation characteristics of low-density high manganese steels, *J. Mater. Sci. Technol.*, 33(2017), No. 12, p. 1531.

[39] J.G. Duh and C.J. Wang, Formation and growth morphology of oxidation-induced ferrite layer in Fe–Mn–Al–Cr–C alloys, *J. Mater. Sci.*, 25(1990), No. 4, p. 2063.

[40] Y.L. Yang, C.H. Yang, S.N. Lin, C.H. Chen, and W.T. Tsai, Effects of Si and its content on the scale formation on hot-rolled steel strips, *Mater. Chem. Phys.*, 112(2008), No. 2, p. 566.

[41] S.H. Park, I.S. Chung, and T.W. Kim, Characterization of the high-temperature oxidation behavior in Fe–25Mn–1.5Al–0.5C alloy, *Oxid. Met.*, 49(1998), No. 3, p. 349.

[42] P.R.S. Jackson and G.R. Wallwork, High temperature oxidation of iron–manganese–aluminum based alloys, *Oxid. Met.*, 21(1984), No. 3, p. 135.

[43] W.S. Yang and C.M. Wan, High temperature studies of Fe–Mn–Al–C alloys with different manganese concentrations in air and nitrogen, *J. Mater. Sci.*, 24(1989), No. 10, p. 3497.

[44] J.L. Sun, B.Y. Huang, J.Q. He, E.C. Meng, and Q.H. Chang, Achieving oxidation protection effect for strips hot rolling via Al$_2$O$_3$ nanofluid lubrication, *Int. J. Miner. Metall. Mater.*, 30(2023), No. 5, p. 908.